ACS Catalysis

Research Article

pubs.acs.org/acscatalysis

Strong Local Coordination Structure Effects on Subnanometer PtO_x Clusters over CeO_2 Nanowires Probed by Low-Temperature CO Oxidation

Jun Ke,[†] Wei Zhu,[†] Yingying Jiang,[§] Rui Si,[*,∥] Yan-Jie Wang,[†] Shuai-Chen Li,[†] Chuanhong Jin,[§] Haichao Liu,[*,‡] Wei-Guo Song,[⊥] Chun-Hua Yan,[†] and Ya-Wen Zhang[*,†]

[†]Beijing National Laboratory for Molecular Sciences (BNLMS), State Key Laboratory of Rare Earth Materials Chemistry and Applications, PKU-HKU Joint Laboratory in Rare Earth Materials and Bioinorganic Chemistry, and [‡]Beijing National Laboratory for Molecular Sciences (BNLMS), State Key Laboratory for Structural Chemistry of Stable and Unstable Species, College of Chemistry and Molecular Engineering, Peking University, Beijing 100871, People's Republic of China

[§]State Key Laboratory of Silicon Materials, Key Laboratory of Advanced Materials and Applications for Batteries of Zhejiang Province, School of Materials Science and Engineering, Zhejiang University, Hangzhou 310027, People's Republic of China

[∥]Shanghai Synchrotron Radiation Facility, Shanghai Institute of Applied Physics, Chinese Academy of Sciences, Shanghai 201204, People's Republic of China

[⊥]Beijing National Laboratory for Molecular Sciences (BNLMS), Institute of Chemistry, Chinese Academy of Sciences, Beijing 100190, People's Republic of China

Supporting Information

ABSTRACT: A fundamental understanding of the structural effects of supported metal catalysts at the molecular level is extremely important for developing high-performance catalysts that are widely used in industry, which is still a longstanding attractive but challenging topic in multidisciplinary fields. In this work, we report the strong effects of local coordination structures on the catalytic activity of subnanometric PtO_x clusters over CeO_2 nanowires in low-temperature CO oxidation as a probe reaction. Atoms and subnanometric clusters of Pt were deposited to form the coordination structure of PtO_x on the well-defined CeO_2 nanowires with mainly exposed (110) facets. The reactivity of active sites and the variation of the local coordination structures of the PtO_x sites were deeply investigated with in situ spectroscopic experiments, assisted by density functional theory simulations. According to our observation, although the highly dispersed Pt sites at the subnanometric scale could provide increased accessible sites, some of the Pt sites did not show high activity for CO oxidation due to the increased surrounding oxygen that seemed to overstabilize the Pt atoms. An increased proportion of both adsorbed CO intermediates on oxidized Pt sites and the interfacial lattice oxygen of PtO_x clusters tended to become inactive on samples with a high coordination number of oxygen bonded to Pt sites (CN(Pt−O)), leading to the loss of effective active sites and a decrease in the catalytic activity. A relatively small CN(Pt−O) value in the subnanometric PtO_x/CeO_2 NWs, which was found to be the appropriate structure for their catalytic performance, remarkably increased the activity by about 1/2 order of magnitude. We believe our investigation on the interfacial coordination structure effects of subnanometric PtO_x clusters dispersed on CeO_2 nanowires can provide some new basic chemical insights into the metal−support interfacial interactions of Pt/CeO_2 catalysts for understanding their catalytic performance in some relevant reactions.

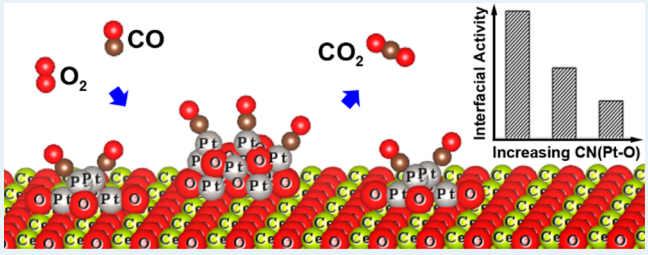

KEYWORDS: *local coordination structure, PtO_x clusters, CeO_2 nanowires, CO oxidation, in situ spectra*

INTRODUCTION

The local structures of active sites are generally important for many heterogeneous catalysts.[1−6] The atoms closely surrounding the active sites can be involved in the catalytic process and influence the catalytic performance of the active sites or their utilization efficiency.[4−6] The highly efficient utilization of supported noble metals, as the most widely used heterogeneous catalysts for many reactions, has attracted both scientific and industrial interest.[7−10] It is thus crucial to understand how the local coordination structure of active sites influences the catalytic property of the supported noble-metal catalysts at the molecular level for rational design of active sites with enhanced activity and maximized metal utilization.

To maximize the number of accessible sites, the noble metals can be dispersed on supports in single atoms or subnanometric

Received: April 22, 2015
Revised: July 18, 2015
Published: July 22, 2015

DOI: 10.1021/acscatal.5b00832
ACS Catal. 2015, 5, 5164−5173

clusters.[1−3,11−15] On reducible oxide supports (e.g., CeO_2, TiO_2, FeO_x), the metal−support interactions involving the transfer of electron and lattice oxygen through an interface can stabilize the highly dispersed metal in its oxidized states with the oxygen linkages and generate active sites.[7,16−25] On inert supports (e.g., SiO_2, Al_2O_3), metal cations can be stabilized by −O and −OH ligands with the assistance of alkali.[1−3,26,27] The highly dispersed metals have relatively uniform local structures of the active sites and exhibit excellent catalytic activity in different reactions, such as CO oxidation and water−gas shift reactions.[11,12,28,29] Recently, Peterson et al. and Yang et al. reported that, in comparison with the catalysts that have just been prepared (Pd−La−Al_2O_3, Pt−Na−TiO_2, Pt−Na−KLTL, and Pt−[Si]MCM41), the coordination number of the metal sites to oxygen decreases at the initial stage of the catalytic reaction when the active structure of the working catalyst forms.[1,2] However, it is unclear whether the activity of the metal catalyst can change with such a slight variation of its local coordination structure and how the support affects the coordination number and consequently the catalytic performance of the metal sites through the metal−support interactions at the atomic level.

Pt/CeO_2 is a representative catalyst with strong metal−support interactions and has many important applications (e.g., in CO oxidations, water−gas shift reactions, and organic synthesis reactions).[28,30−32] Ceria, especially ceria nanocrystals with a well-defined morphology, provides variable-valence Ce ions and active lattice oxygen atoms for charge transfer and oxygen migration between the metal and the ceria support.[30,33−39] It has been reported that electrons can transfer from Pt to ceria and that Pt particles below 2−3 nm mainly have positive valence.[18,28] DFT simulations show that oxygen can spill over from ceria to Pt.[18,40] As probed by CO oxidation and water−gas shift reactions, the Pt cations at the interface can result in relatively weak Pt−CO bonds and enhanced oxygen reducibility and are thus regarded as the active sites.[41−43] Moveover, it is also found that, for CO oxidation, the Pt nanoparticles on CeO_2 can show very high activity with mechanistic features similar to those of some single-atom metal catalysts, especially at low temperatures.[44,45] This is in agreement with observations in the literature that, in addition to the size of Pt nanoparticles (or clusters), some other factors, such as valence distribution, surface morphology of ceria, and the oxygen defects of the support, can also influence the proportion of interfacial sites and the activity at relatively low temperatures (30−80 °C), although the underlying reasons need to be clarified at the atomic level.[46−49]

Herein, we demonstrate the strong effects of the local coordination structures of subnanometric PtO_x clusters over CeO_2 nanowires on their catalytic properties in low-temperature CO oxidation as a probe reaction. We chose (110)-exposed CeO_2 nanowires (NWs) with well-defined surface structure as the support.[6] Pt was deposited to form PtO_x clusters at the subnanometer scale as the interfacial sites. Subnano PtO_x/CeO_2 NWs with varied local coordination structures were studied by in situ spectroscopic experiments and density functional theory (DFT) calculations in order to reveal the relationship between the reactivity of the PtO_x sites and their local structures that govern the catalytic process of CO oxidation at low temperatures.

EXPERIMENTAL SECTION

$CeCl_3·7H_2O$ (AR, Sinopharm Chemical Corp., People's Republic of China), K_2PtCl_4 (AR, Sinopharm Chemical Corp., People's Republic of China), NaCl (AR), NaOH (AR), $Ce(NO_3)_3·6H_2O$ (AR, Xilong Chemical Corp., People's Republic of China), and $NaBH_4$ (AR) were used as the starting materials.

Synthesis of PtO_x/CeO_2 NWs. Ceria nanowires were obtained by the reported hydrothermal method.[6] A 279 mg portion of $CeCl_3·7H_2O$, 3.6 g of NaOH, and 0.523 g of NaCl were dissolved and mixed in 15 mL of water. The suspension was placed in a 25 mL Teflon-lined autoclave and heated at 180 °C for 24 h. The nanowires were collected by centrifugation and washed three times with deionized water. Then, the samples were dried at 200 °C overnight. Annealed CeO_2 NWs were made by heating the ceria NWs at 600 °C for 3 h (ramping rate 10 °C·min^{-1}) and then cooling at a rate of 1 °C/min.

A 130 mg portion of the above CeO_2 NWs were dispersed in 10 mL of water with ultrasonic treatment. A 156−1250 μL portion of K_2PtCl_4 solution (0.024 mol L^{-1}) was mixed. The suspension was stirred at room temperature for 2 h. The products were washed with deionized water at least three times and then dried at 70 °C overnight. The as-obtained supported NWs were reduced in H_2 at 140 °C for 10 min to obtain the sample, denoted as PtO_x/CeO_2 NWs-140. The supported NWs were reduced in H_2 at 350 °C for 120 min to obtain a sample denoted as PtO_x/CeO_2 NWs-350. The products were exposed to air after they were cooled naturally to room temperature. The as-obtained PtO_x/CeO_2 NWs-350 were treated in CO and O_2 at 150 °C for 30 min to obtain samples denoted as PtO_x/CeO_2 NWs-350 (less O) and PtO_x/CeO_2 NWs-350 (more O), respectively. Samples denoted as Pt/CeO_2 NWs were obtained by adding $NaBH_4$ solutions to the suspension with K_2PtCl_4 solution during Pt deposition, and other steps were similar to those for Pt deposition on ceria NWs.

Instrumentation. Pt loading was analyzed from inductively coupled plasma atomic emission spectroscopy (ICP-AES) carried out on Profile Spec ICP-AES spectrometer (Leeman, USA). Transmission electron microscopy (TEM) images were obtained on a JEM-2100F field emission TEM (JEOL, Japan). High angular annular dark field scanning transmission electron microscopy (HAADF-STEM) images were obtained from an FEI TITAN aberration-corrected ChemiSTEM operated at 200 kV, which incorporated a probe corrector. Dilute suspensions of our samples in ethanol were dropped on copper grids coated with amorphous carbon membranes and dried for TEM and STEM observations. X-ray photoelectron spectroscopy (XPS) data were obtained with an Axis Ultra XPS spectrometer (Kratos, U.K.) with Al Kα radiation operated at 225 W. The binding energy was calibrated by the peak at 284.8 eV in the C 1s spectra. The Brunauer−Emmett−Teller (BET) surface area was analyzed on an ASAP-2010 gas sorption instrument (Micromeritics, USA) via the physical adsorption of nitrogen at 77 K. The samples were pretreated at 150 °C under vacuum before analysis.

Extended X-ray absorption fine structure (EXAFS) analysis of the Pt L_3 edge (11564 eV) was conducted on the 1W2B beamline of the Beijing Synchrotron Radiation Facility (BSRF) at 2.2 GeV with injection currents of 300−500 mA and on the BL14W1 beamline of Shanghai Synchrotron Radiation Facility (SSRF) at 3.5 GeV under top-up mode with a current of 220 mA. The spectra of Pt foils and bulk PtO_2 as the reference samples were collected in transmission mode. The spectra of ceria-supported Pt samples were obtained in fluorescence mode by Lytle detectors at the BSRF and 32-channel Ge solid state detector at the SSRF. The spectrum of each sample was collected several times to improve the quality of the data. In situ EXAFS and X-ray absorption near edge structure (XANES) analysis was performed at the X18B beamline of the National Synchrotron Light Source

DOI: 10.1021/acscatal.5b00832
ACS Catal. 2015, 5, 5164−5173

(NSLS) at Brookhaven National Laboratory (BNL) in decay mode with currents of 160−300 mA. The Pt L_3 edge of the Pt−ceria samples was measured in fluorescence mode with a four-channel Vortex silicon drift detector. The experiments were carried out under CO oxidation conditions (2% CO/5% O_2/He, 20 mL/min, 75 °C), and the outlet gas mixture was analyzed by a mass spectrometer (MS). Athena software was used for the data extraction and for the curve fitting of XANES profiles with linear combination analysis. Artemis software was used to fit the EXAFS curves of k^2-weighted Pt spectra in real space with Δk = 2.6−10 Å^{-1} and ΔR = 1.2−3.3 Å.

CO and H_2 chemisorption was performed on a Quantachrome autosorb-iQ instrument at 20 °C. The samples were reduced under flowing 8% H_2/Ar at 300 °C for 1 h and evacuated at 300 °C for 4 h before measurements.[45] Pt dispersion was analyzed by assuming 1:1 H:Pt and CO:Pt adsorption stoichiometry. Temperature-programmed hydrogen reduction (H_2-TPR) was analyzed on a Quantachrome autosorb-iQ instrument by heating the samples (50 mg) to 900 °C (5 °C/min) under 30 mL/min of flowing 8% H_2/Ar. A thermal conductivity detector (TCD) was equipped to analyze the H_2 consumption. The samples were pretreated under flowing He at 50 °C for 60 min before measurements.

In situ IR spectra in diffuse reflectance mode (DRIFTS) were measured on a Bruker TENSOR 27 spectrometer. The samples were exposed to a gas flow (40 mL/min) in a Praying Mantis DRIFTS cell. The gas mixture was switched among 2% CO/5% O_2/He, 5% CO/He, and 5% O_2/He.

Catalytic Tests. The catalytic activities of CO oxidation over the samples were evaluated in a fixed bed reactor at 1 atm. The sample (50−500 mg) was mixed with quartz sand and then placed in a quartz tube. The reactant gas was a mixture of CO (2 mL/min), O_2 (5 mL/min), and He (8 mL/min). The online analysis of the outlet gas mixture was performed on an Agilent 7890A gas chromatograph equipped with a TCD detector and a carbon molecular sieve column (Carboxen 1000, Supelco, USA). The temperature was ramped at 2 °C/min, and the required temperature was maintained for 2 h before the data were collected. The dependence of the activity on the partial pressure of the reactants was examined by varying the flow rate of each reactant. The total pressure was kept at 1 atm with the balance of He. The conversion of each reactant was controlled below 15%.

First-Principles Calculations. Density functional theory (DFT) calculations were performed with VASP software. Spin-polarized Kohn−Sham equations were expanded into plain waves. The exchange−correlation energy functional was described in the Perdew−Burke−Ernzerhof (PBE) generalized gradient approximation (GGA). In the Brillouin zone, the k point was set to the Gamma point. The atoms were presented by projector augmented-wave (PAW) pseudopotentials. The kinetic energy cutoff was 500 eV for the plane-wave basis set. CeO_2 supercells (4 × 4 × 5) with exposed (110) surfaces were built. Two layers were fixed in the supercell, and 15 Å of vacuum was added. U = 5 eV on the Ce 4f orbital was added.[50−52] Pt and CO were placed on the surface. Each structure was relaxed until the residual force was smaller than 0.02 eV/Å.

RESULTS AND DISCUSSION

Preparation of CeO_2 NWs Loaded with PtO_x Clusters on a Subnano Scale. Atoms and subnano clusters of Pt were deposited onto the CeO_2 NWs by the conventional wet impregnation method in water. Within 2 h of deposition, with an increasing amount of the Pt precursor added, the quickly deposited Pt appeared to reach a saturated coverage on the NWs (Figure S1 in the Supporting Information). Weakly adsorbed Pt and other ions were washed away with water several times to ensure strong Pt deposition with high dispersion onto the ceria NWs, followed by centrifugal separation and drying in ambient air. Then, PtO_x/CeO_2 NWs were obtained after H_2 treatment. The samples treated at low temperatures (e.g., 140 °C) and at high temperatures (e.g., 350 °C) under H_2 are denoted as PtO_x/CeO_2 NWs-140 and PtO_x/CeO_2 NWs-350 (Figure 1 and Figures S2−S4 in the Supporting Information), respectively.

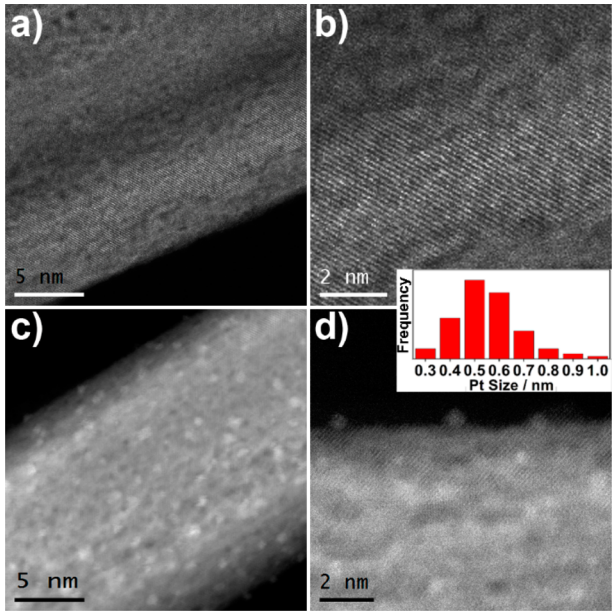

Figure 1. Aberration-corrected STEM images of 1.3% PtO_x/CeO_2 NWs-140 (a, b) and 1.3% PtO_x/CeO_2 NWs-350 (c, d). The insert in panel d shows the size distribution of PtO_x clusters on the sample of 1.3% PtO_x/CeO_2 NWs-350 obtained from measurements of the size of over 150 nanoclusters.

For the sample of 1.3% PtO_x/CeO_2 NWs-140 (1.3% was the weight percentage of Pt from ICP-AES analysis), TEM and aberration-corrected STEM images (Figure 1a,b) show that very few particles up to 0.4 nm in hemispherical or truncated polyhedral shapes were found, indicating that most of the Pt atoms were atomically dispersed and directly bonded to the surface of the ceria NWs (Table S1 in the Supporting Information). According to the EXAFS data (Figure S5 and Table S2 in the Supporting Information), the coordination number (CN) of Pt−Pt was unable to be clearly fitted. The CN(Pt−O) value was 3.8 ± 0.2 (Table 1), indicating that Pt was in the form of PtO_x clusters.

For a sample treated in H_2 at higher temperature (e.g., 350 °C), Pt could grow up to subnano clusters. On the surface of the sample of 1.3% PtO_x/CeO_2 NWs-350, as shown in Figure 1c,d, the size of PtO_x clusters was mainly 0.5 ± 0.1 nm (it was possible that the STEM images could miss some PtO_x clusters at smaller scales, including single-atom PtO_x clusters, because of the similar Z^2 values for Ce and Pt). The average distance between each cluster was about 2−4 nm, which agreed with the Pt coverage and the cluster size. The CN(Pt−O) value decreased to 2.6 ± 0.3 in the PtO_x clusters. However, the CN(Pt−Pt) value was still negligible, indicating that the Pt−Pt bonds were disordered or hardly formed. These structural features suggested that the Pt atoms in subnanometer PtO_x clusters were similar to the "pseudo

DOI: 10.1021/acscatal.5b00832
ACS Catal. 2015, 5, 5164−5173

Table 1. EXAFS Parameters for PtO_x/CeO_2 NWs

sample	shell	CN
0.42% PtO_x/CeO_2 NWs-350	Pt−O	2.5 ± 0.9
0.78% PtO_x/CeO_2 NWs-350	Pt−O	2.5 ± 0.6
1.3% PtO_x/CeO_2 NWs-350	Pt−O	2.6 ± 0.3
2.1% PtO_x/CeO_2 NWs-350	Pt−O	2.5 ± 0.3
1.3% PtO_x/CeO_2 NWs-140	Pt−O	3.8 ± 0.3
1.3% PtO_x/CeO_2 NWs-350 (less O)	Pt−O	2.0 ± 0.3
1.3% PtO_x/CeO_2 NWs-350 (more O)	Pt−O	3.1 ± 0.3
1.3% Pt/CeO_2 NWs	Pt−O	0.7 ± 0.4
	Pt−Pt	7.6 ± 0.8

single atoms" in some reports.[14] For a sample of 0.42% PtO_x/CeO_2 NWs-350, the average cluster size and the coordination structure of Pt were similar.

For comparison, a sample of Pt/CeO_2 NWs with large Pt particles was obtained from quick reduction of K_2PtCl_4 with $NaBH_4$ during Pt deposition (denoted as Pt/CeO_2 NWs). The sizes of Pt particles were mainly 10−25 nm (Figure S6 in the Supporting Information). The particles seemed to appear the shapes similar to the aggregation of smaller particles with irregular shapes that was as small as 2−4 nm (the primary particle size). For this sample, CN(Pt−Pt) increased obviously to 7.6 ± 0.8, which agreed with the primary particle size. The CN(Pt−O) value decreased to 0.7 ± 0.4. Among the samples mentioned above, the CN(Pt−O) increased with decreasing Pt cluster (or particle) size. For samples of PtO_x/CeO_2 NWs, the high dispersity of Pt species allowed maximum contact with the oxygen both on ceria and in air.[18,53] With the assistance of electron transfer from Pt atoms to ceria, the lattice oxygen atoms on ceria could spill over quickly to the Pt atoms in oxidized states and get replenished from O_2 in air, which caused the high CN(Pt−O) values at the Pt−O_x−Ce sites in the samples of PtO_x/CeO_2 NWs.

For all of the samples of PtO_x/CeO_2 NWs, XPS Pt 4f spectra showed that Pt was mainly in the +2 state (Figure S7 and Table S3 in the Supporting Information). The percentage of Pt(0) on the sample of 1.3% Pt/CeO_2 NWs increased slightly due to the increased size of the particles.[28] XPS Ce 3d spectra show that Ce^{3+} was undetectable on the surfaces of all of the samples (Table S4 and Figure S8 in the Supporting Information), probably due to the fast O_2 replenishment ability of CeO_2 NWs, which was different from the case of Pt/CeO_2 grown under ultrahigh-vacuum conditions.[47]

Catalytic Activity in CO Oxidation. The turnover frequency (TOF) value (normalized to the value per exposed surface Pt atom) of catalytic CO oxidation over 1.3% PtO_x/CeO_2 NWs-140 was less than 10^{-4} s^{-1} at 50 °C. The TOF values of 0.42−2.1% PtO_x/CeO_2 NWs-350 were (1.3−1.1) × 10^{-2} s^{-1} (Figure 2 and Table S5 in the Supporting Information), which were approximately 1 order of magnitude higher than that of the sample of 1.3% Pt/CeO_2 NWs. The valences of Ce and Pt, the sizes of PtO_x clusters, and the exposed facets of the samples of PtO_x/CeO_2 NWs-350 did not change much after the catalytic tests (Tables S1 and S6 and Figures S9 and S10 in the Supporting Information).

The apparent activation energies for the samples of PtO_x/CeO_2 NWs-350 and Pt/CeO_2 NWs were similar (65−70 kJ mol^{-1}) (Table S7 in the Supporting Information), suggesting that a similar reaction pathway might be followed for these samples. The difference in their activity was considered to mainly come from the different numbers of effective active sites (rather than the exposed sites), which agreed with the previous reports.[45]

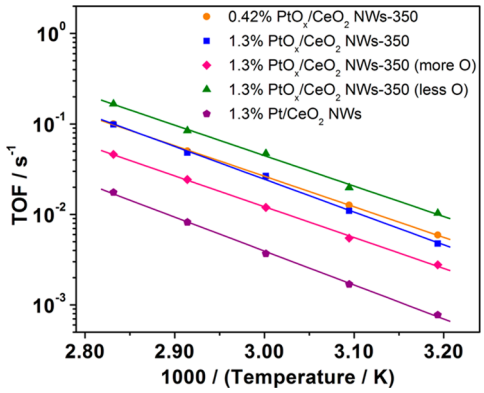

Figure 2. Catalytic activity on CO oxidation over PtO_x/CeO_2 NWs. Error bounds are estimated to be about ±20%. The TOF value of 1.3% PtO_x/CeO_2 NWs-140 was less than 10^{-4} s^{-1} at 50 °C. The TOF value of the pure support CeO_2 NWs was 4.1 × 10^{-5} s^{-1} at 200 °C.

When the partial pressure of CO or O_2 varied slightly, TOF values of these samples did not obviously change (Figure S11 in the Supporting Information).[45,49,54,55] This result suggested that CO adsorption and lattice oxygen replenishment were fast steps and that the rate-determining step should be the reaction of adsorbed CO with oxygen species at the Pt−O_x−CeO_2 interface, as reported previously.[45] The active sites were at the interface of Pt and ceria.[45] However, the activity of 1.3% PtO_x/CeO_2 NWs-140 was very low, in spite of the high proportion of interfacial Pt atoms. The proportion of active interfacial Pt sites seemed to be higher in PtO_x/CeO_2 NWs-350 with subnano PtO_x clusters than in 1.3% PtO_x/CeO_2 NWs-140 with more highly dispersed Pt atoms. Therefore, some other factors were thought to cause the loss of active Pt sites in addition to the particle/cluster size. The oxygen defects, adsorbed hydroxyls and water, and residual surface Cl on the CeO_2 NWs support were excluded as the major reason for the difference in activities among our samples (see Figure S12 and the related discussion in the Supporting Information). The 1.3% Pt/CeO_2 NWs-350 sample was chosen as the representative for further study.

Reactivity of Lattice Oxygen of PtO_x Clusters at Interface. The role of interfacial lattice oxygen on 1.3% PtO_x/CeO_2 NWs-350 was evaluated from the pulse injection of CO.[13,41] As shown in Figure S13 in the Supporting Information, the sample was first stabilized in a mixture of CO and O_2, similar to the steady-state reaction conditions. Then, the gas was switched to CO of the same concentration. The amount of CO_2 produced remained at about 70% in the first pulse of CO, in comparison to that obtained in the presence of O_2 coreactant, and gradually decreased in the following pulses with depletion of the lattice oxygen. CO conversion could recover quickly and completely after the injection gas was switched back to the CO oxidation conditions by introducing gaseous O_2. These results clearly revealed the involvement of interfacial lattice oxygen of PtO_x clusters in the CO oxidation to CO_2 proceeding via a Mars−van Krevelen mechanism. Oxygen consumption in the initial five CO pulses was 26 μmol g_{cat}^{-1}, corresponding to a O:Pt ratio of 0.4:1, which indicates that only a part of the oxygen very close to Pt (mainly in the Pt−O_x−Ce linkages) was involved in this step at 50 °C (Figures S13 and S14 in the Supporting Information).

The activity of lattice oxygen of the PtO_x clusters could be further estimated according to the reducibility of PtO_x sites from H_2-TPR analysis. The H_2 consumptions below 200 °C, around

DOI: 10.1021/acscatal.5b00832
ACS Catal. 2015, 5, 5164−5173

350−550 °C, and above 700 °C were attributed to the reduction of oxygen close to the Pt−ceria interface, surface oxygen on ceria, and bulk oxygen, respectively (Figure 3).[30,49,56] The first H_2

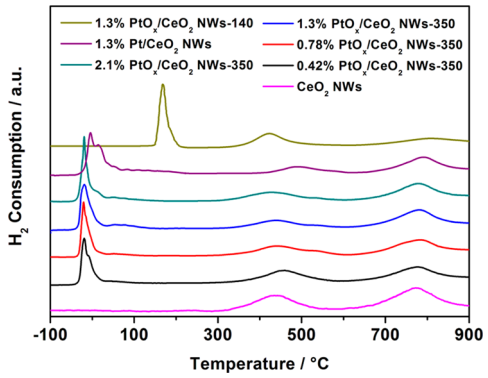

Figure 3. H_2-TPR profiles of PtO_x/CeO_2 NWs samples.

consumption peak represented the reduction of PtO_x, and consequent hydrogen spillover from the reduced Pt sites to ceria caused the reduction of surface oxygen of ceria with the concurrent formation of OH species (Figure S15 in the Supporting Information), according to previous reports.[57] This peak appeared at 160 °C for the sample of PtO_x/CeO_2 NWs-140, similar to that in some previous reports.[30] CO-TPR analysis also showed the relatively low reducibility of PtO_x sites on this sample (Figure S14 in the Supporting Information). Obvious H_2 consumption was observed at about −25 and 0 °C on the samples of PtO_x/CeO_2 NWs-350 and Pt/CeO_2 NWs, respectively.

The sequence of the reducibility agreed with the sequence of their catalytic activity, indicating that the reducibility of PtO_x clusters at the Pt−CeO_2 interface played an important role in CO oxidation. In the sample of 1.3% PtO_x/CeO_2 NWs-140 with the highest CN(Pt−O), Pt cations were tightly anchored on the ceria support.[25] This sample had a very low lattice oxygen reducibility at Pt−O_x−Ce sites; thus, the amount of active sites became very small, leading to the low catalytic activity. Pt atoms in 1.3% PtO_x/CeO_2 NWs-350 were more highly dispersed and more densely located on the NWs; therefore, they could provide more active sites to activate the interfacial lattice oxygen than could the Pt atoms in 1.3% Pt/CeO_2 NWs. For the sample of 0.42−2.1% PtO_x/CeO_2 NWs-350 with a similar coordination environment of PtO_x clusters, the reducibility of the oxygen at PtO_x sites was similar, which agreed with their similar catalytic activity.

Reactivity of Adsorbed CO Intermediates on PtO_x Sites. In situ IR analyses were performed to investigate the active sites of the PtO_x clusters for CO adsorption during the catalytic process and to evaluate the reactivity of these adsorbed CO intermediates. The weak absorbance peaks (Figure S16 and Table S8 in the Supporting Information) around 2172 and 1833 cm^{-1} were assigned to the vibration of gaseous CO and bridge-bonded CO, respectively.[58−61] The peaks at 2120−2066 cm^{-1} were attributed to the linearly adsorbed CO on Pt^{2+} (oxygen on Pt), $Pt^{\delta+}$ (oxygen on neighboring Pt), and Pt^0 sites.[58−60,62−65] The vibration of linearly adsorbed CO with relatively smaller wavenumbers was attributed to the stronger CO bonding to the Pt sites with lower CN(Pt−O) (valence) or lower CN(Pt−Pt) values (coordinatively unsaturated sites).[62]

During CO oxidation over 1.3% PtO_x/CeO_2 NWs-350, linear CO adsorption on Pt^{2+} (2102 cm^{-1}) and $Pt^{\delta+}$ (2088 cm^{-1}) became saturated quickly in the initial 1−2 min (Figure S16 in the Supporting Information). The absorbance of CO on the Pt sites at 2075 cm^{-1} (Pt^0) gradually increased in the first 30 min due to the partial reduction of the PtO_x clusters, which was similar to the finding in previous studies.[59,64] After 5 h of reaction, the peak at 2088 cm^{-1} gradually shifted to a higher wavenumber (2096 cm^{-1}), which was attributed to more oxidized sites, suggesting the structural variation of partial Pt sites. On PtO_x/CeO_2 NWs-140 (the black curve in Figure 4b), CO mainly

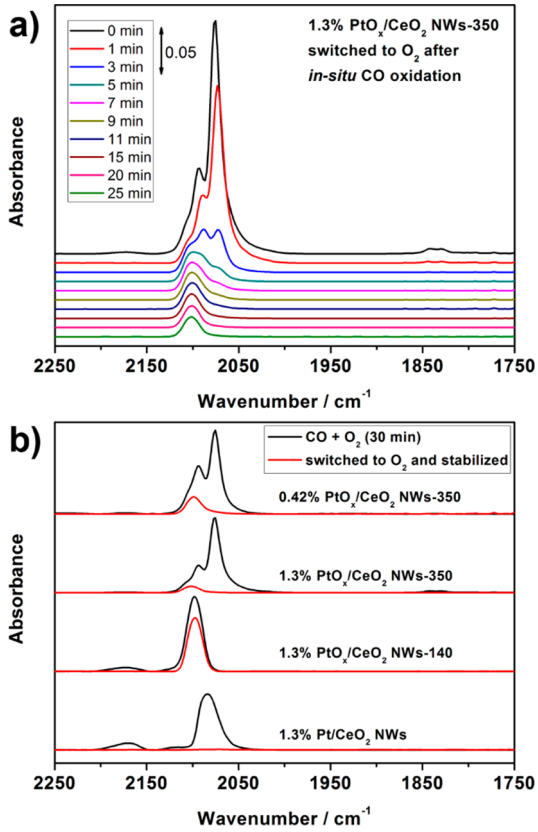

Figure 4. In situ IR spectra of PtO_x/CeO_2 NWs under CO oxidation conditions: (a) reaction of adsorbed CO intermediates with O_2 over a sample of 1.3% PtO_x/CeO_2 NWs-350 after stabilization under the CO oxidation conditions; (b) stabilized peaks under CO oxidation conditions and the residual peaks after O_2 treatment for the PtO_x/CeO_2 samples.

adsorbed on Pt^{2+} and $Pt^{\delta+}$ sites (around 2098 cm^{-1}),[58,59] which agreed with the XPS data (showing Pt existed mainly in the oxidized states). On Pt/CeO_2 NWs with large Pt particles (the black curve in Figure 4b), the peak appeared around 2085 cm^{-1}, attributed to the CO adsorption mainly on Pt^0 and $Pt^{\delta+}$ sites.[58,62]

When the sample of 1.3% PtO_x/CeO_2 NWs-350 almost became stabilized in the mixture of CO and O_2 as the steady-state reaction, the reactant flow was switched to O_2 to evaluate the reactivity of adsorbed CO intermediates (Figure 4a). The peaks of linearly adsorbed CO on Pt^{2+}, $Pt^{\delta+}$, and Pt^0 sites were fitted with Gaussian peaks for the variation of their relative amounts (Figure S17 in the Supporting Information). In most of the spectra along the reaction time, residual percentages of the peak at lower wavenumbers were smaller. After the intensity of the peaks almost did not decrease, the peak assigned to Pt^0 disappeared. The residual absorbances of CO on Pt^{2+} and $Pt^{\delta+}$ were approximately 66% and less than 15%, respectively (Figure S17),

DOI: 10.1021/acscatal.5b00832
ACS Catal. 2015, 5, 5164−5173

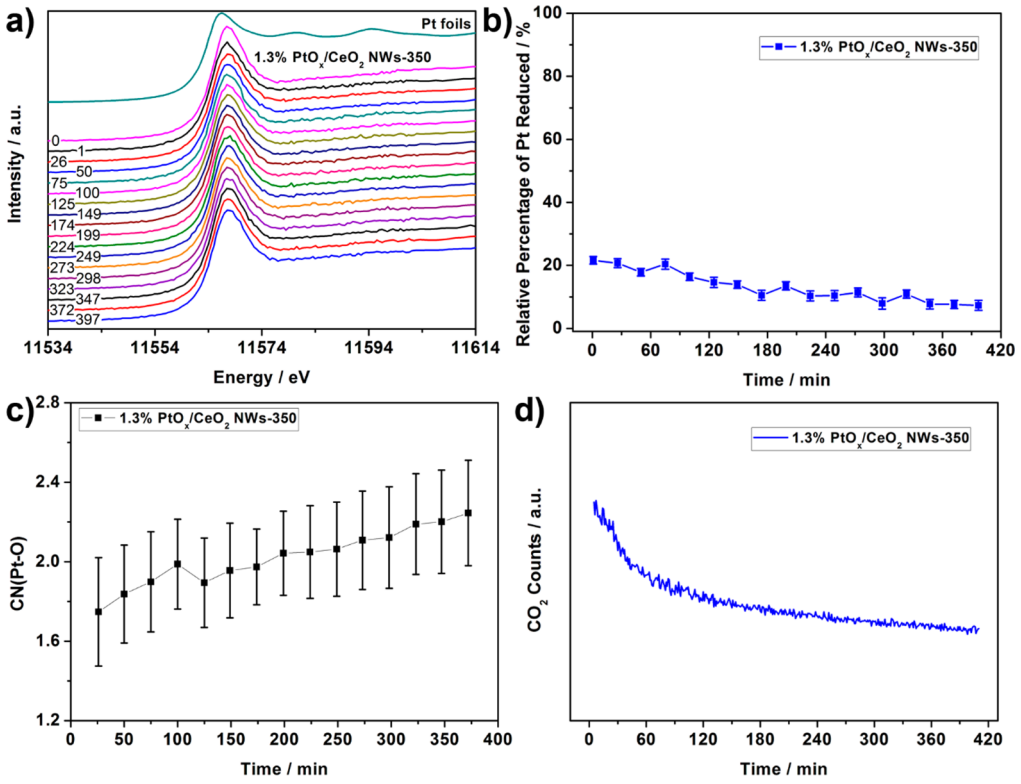

Figure 5. In situ EXAFS and XANES analysis of the sample of 1.3% PtO_x/CeO_2 NWs-350 under CO oxidation conditions. The collection of each spectrum lasted about 24 min. (a) In situ XANES spectra. The values given in the spectra represent the time (in min) when the collection of spectra started during the in situ CO oxidation. (b) Linear combination analysis of the in situ XANES spectra with the fitting error. The XANES spectra were fitted as a linear combination of the Pt foil spectra and the spectra of the 1.3% PtO_x/CeO_2 NWs-350 sample at 0 min (Figure S18 in the Supporting Information). The relative percentage of Pt reduced represents the fitted coefficient of Pt foils. (c) Fitting results of the CN(Pt−O) values with the fitting error along the reaction time according to the in situ EXAFS spectra. Each spectrum was averaged with the neighboring spectra before the Fourier transforms and the fitting. (d) CO_2 evolution during in situ analysis obtained from MS signals.

which represented the most inactive sites. The proportion of inactive sites for the oxidized Pt^{2+} sites (with more coordinated oxygen present) was the highest in comparison to Pt^0 and $Pt^{\delta+}$ sites.

For the samples of 1.3% PtO_x/CeO_2 NWs-140 and Pt/CeO_2 NWs, the residual absorbances of CO on inactive sites were about 71% and 1%, respectively (Figure 4b). For the three samples, with an increase in the average CN(Pt−O), the proportion of inactive sites with adsorbed unreactive CO intermediates increased, indicating that the coordinated oxygen probably made the Pt sites inactive. This trend agreed with the sequence of the proportion of effective active sites at the Pt−CeO_2 interface according to the catalytic tests. According to the reports for the supported metal cations, the Pt cations can weaken the Pt−CO bonds and enhance the activity.[42,43] However, the Pt sites with highly coordinated oxygen appeared to show relatively low activity for our subnano PtO_x/CeO_2 samples. These observations were apparently quite similar to the reports on the activity of metallic sites for metallic metal nanoparticles on ceria.[30,46,66]

Influence of Coordination Environment of Subnano PtO_x Clusters. In situ XANES and EXAFS analyses were carried out to evaluate the change in the valence and the coordination structure of 1.3% PtO_x/CeO_2 NWs-350 during CO oxidation. According to a linear combination fitting of the in situ XANES spectra (Figure 5 and Figure S18 in the Supporting Information), most of the Pt sites retained their initial oxidized state during the catalytic process. Small parts of the Pt sites were reduced at the beginning of the catalytic reaction (Figure 5b), which was consistent with the variation of the peak assigned to Pt^0 sites in the initial minutes of the in situ IR spectra (Figure S16 in the Supporting Information), probably due to the adsorption of CO and its reaction with part of the oxygen in the PtO_x clusters. The percentage of reduced Pt sites gradually decreased in the following several hours of the reaction before stabilization, which agreed with the blue shift of the $Pt^{\delta+}$ peak in the in situ IR spectra (Figure S16).

In situ EXAFS spectra (Figure S19 in the Supporting Information) show that the coordination structure of PtO_x clusters in the sample of 1.3% PtO_x/CeO_2 NWs-350 did not undergo significant changes during CO oxidation, and thus the Pt sites were still mainly highly coordinated with oxygen. The Pt−Pt shell was still unable to be clearly fitted from the EXAFS spectra. The CN(Pt−O) value gradually increased during the reaction (Figure 5c and Table S9 in the Supporting Information), indicating that the Pt sites in subnano clusters preferred to bond with oxygen under the CO oxidation conditions. This was in accordance with the variation of Pt valence according to the in situ XANES results. The CO oxidation activity decreased dramatically (by about 45%) in the initial 2 h of the in situ observation (Figure 5d), and the samples retained most of their activity in the following 5 h. From a consideration of the fact that the surface morphology did not change significantly after the reaction (Figure S10 in the Supporting Information), the increase in oxidized Pt sites and CN(Pt−O) values seemed to be one of the main reasons that caused a decrease in the amount

DOI: 10.1021/acscatal.5b00832
ACS Catal. 2015, 5, 5164−5173

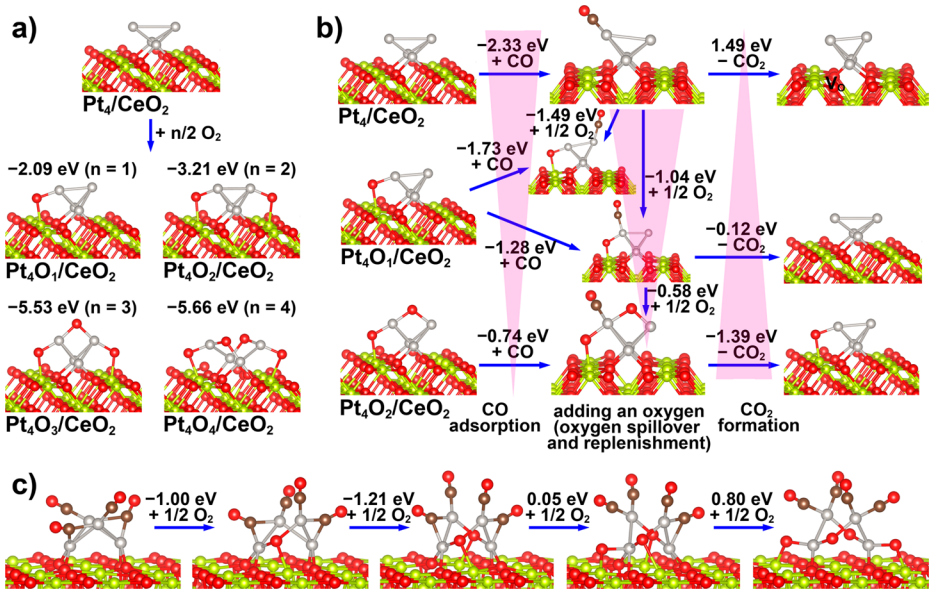

Figure 6. DFT simulation of Pt_4O_x clusters with coordinated oxygen and CO adsorption on CeO_2 (110) surfaces. The yellow, red, light gray, and dark brown balls represent Ce, O, Pt, and C, respectively. (a) Pt_4O_x (x = 0−4) clusters on ceria (110) surfaces. (b) CO adsorption, bonding of an additional oxygen (oxygen spillover and replenishment), and CO_2 formation on a selected Pt with varied coordinated oxygen. The pink spirelike triangles indicate the variation trends. (c) Simulation of 1:1 CO adsorption and addition of an additional interfacial oxygen on Pt_4O_x clusters with varied CN(Pt−O) values.

of effective active sites and thus the catalytic activity, which agreed with the observed relation between high CN(Pt−O) and inactive sites revealed from the in situ IR spectra.

To further reveal the influence of coordination structure of the Pt sites on the catalytic performance of the subnano PtO_x/CeO_2 NWs, the CN(Pt−O) value was slightly adjusted through CO or O_2 treatments before the catalytic tests. The activity of samples with less and more oxygen coordination became about 2 times of that and 1/2 of that for the untreated sample (Figure 2 and Table S5 in the Supporting Information), respectively (Figures S20 and S21 in the Supporting Information for H_2-TPR and in situ IR analysis). Consecutive redox treatment of the sample of PtO_x/CeO_2 NWs-350 also resulted in a similar variation trend in its activity (Figure S22 in the Supporting Information).

DFT Understanding of the Reactivity of PtO_x Clusters. The Pt_4O_x clusters and single Pt atom (Pt_1O_x) with varied CN(Pt−O) values were built on a CeO_2 (110) surface to represent the subnano clusters and the pseudo single atoms of Pt to perform the simulations (Figure 6 and Figure S23 in the Supporting Information). The energy of the models has been reported to be sensitive to the cluster structure; thus, the great variation of structure was avoided during the simulations to reveal the variation trends.[67] The bonding site for single Pt atoms (O-bridge site, Figure S22 in the Supporting Information) agreed with the reported models.[68] The CN(Pt−O) values were 2−4 for these Pt_1O_x models, which were similar to those extracted from the EXAFS data. The formation energy for the Pt_4 cluster to bond one to four oxygen atoms was −2.09 to −5.66 eV, indicating the favorable formation of Pt_4O_x clusters. The size of four Pt atoms in Pt_4O_x (x = 0−4) clusters was in the range of about 0.4−0.7 nm when the radii of Pt atoms were taken into account. This size was similar to the average size of the PtO_x clusters (0.5 ± 0.1 nm) shown in the STEM images. The coordination number of the Pt_4O_x clusters varied from CN(Pt−Pt) = 2 and CN(Pt−O) = 1 for Pt_4O_0 to CN(Pt−Pt) = 1 and CN(Pt−O) = 2.5 for Pt_4O_4 (only the Pt−Pt bond with a bond length close to 0.275 nm was counted). The Pt−Pt distance between each Pt atom ranged from 2.58 to 4.03 Å. The coordination structures of these models were very close to those deduced from the EXAFS data (the average value contributed from pseudo single atoms and clusters of Pt), CN(Pt−O) = 1.7−3.8, and the Pt−Pt shell was unable to be clearly fitted (low CN value or the bond length was not highly ordered). Therefore, the models of Pt_4O_x and Pt_1O_x clusters showed structural features similar to those in the experiments and could be representative in performing the DFT calculations.

Simulations on Pt_4O_x and Pt_1O_x clusters with different CN(Pt−O) values were performed to understand the variation trends during the interaction of CO and oxygen with PtO_x sites. On a selected Pt of Pt_4O_x clusters with zero, one, and two coordinated oxygen atoms (Figure 6b), the CO adsorption energies were −2.33, −1.28, and −0.74 eV, respectively, indicating a decreasing CO adsorption tendency with the increasing coordinated oxygen. On the Pt_4 cluster with one oxygen, the CO adsorption favored the Pt with no bonded oxygen (−1.73 eV) more than that with one coordinated oxygen (−1.28 eV). The CO_2 formation energies were 1.49, 0.12, and −1.39 eV for the adsorbed CO on the selected Pt with zero, one, and two coordinated oxygens, respectively. CO_2 formed more easily on PtO_x with coordinated oxygen than on the metallic Pt clusters.

The formation of active coordinated oxygen was simulated from binding with an additional oxygen atom on the clusters, which could be regarded as either direct oxidation or a combination of oxygen spillover and consequent fast O_2 replenishment through ceria surface during the catalytic process according to the reported simulations.[34,40] This step was simulated on the Pt clusters with adsorbed CO. The energy for bonding one additional oxygen to both the selected Pt (Figure 6b) and the Pt_4O_x clusters with 1:1 CO adsorption (Figure 6c) decreased with an increasing number of oxygens on Pt_4O_x clusters, indicating that the PtO_x clusters lost their active interfacial

DOI: 10.1021/acscatal.5b00832
ACS Catal. 2015, 5, 5164−5173

oxygen species with an increasing CN(Pt−O) value. On the Pt_4O_x clusters with 1:1 CO adsorption, when the interfacial oxygen increased, only the two Pt atoms at the top side were favorable in bonding the adsorbed CO, which suggested that the CO adsorption sites decreased on the PtO_x clusters with high CN(Pt−O) values. Therefore, although CO_2 formation was facilitated on PtO_x clusters with interfacial oxygen, the Pt sites with high CN(Pt−O) values could also lose a part of the active sites because of the loss of suitable CO adsorption sites and the loss of active interfacial oxygen. A similar tendency was also found from the simulation of single Pt atoms on the CeO_2 (110) surface (Figure S23 in the Supporting Information).

Discussions on the Effects of Coordination Structure of PtO_x Sites. On the basis of the results of the above experiments and simulations, the catalytic performances of the subnano PtO_x clusters on CeO_2 NWs were closely related to their two structural features, including the subnano cluster size with relatively high Pt dispersion and the Pt sites highly coordinated with oxygen, during the catalytic process. The two features significantly affected the proportion of suitable active sites for the reaction between adsorbed CO and the interfacial oxygen coordinated to Pt sites. It is known that, for subnano PtO_x/CeO_2 NWs, the subnanometric clusters provided increased exposed Pt sites and interfacial sites for the reaction at the Pt−CeO_2 interface in comparison to Pt/CeO_2 NWs with large Pt particles. The densely dispersed subnano PtO_x clusters could activate their surrounding lattice oxygens bonded to Pt atoms according to H_2-TPR analysis, which brought benefits to their catalytic activity. Meanwhile, the coordinated oxygens around Pt sites, as depicted in Figure 7, could cause the loss of active sites. The

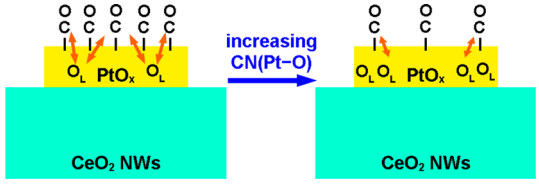

Figure 7. Proposed effects of the increasing CN(Pt−O) on the low-temperature catalytic CO oxidation over subnano PtO_x/CeO_2 NWs. O_L represents the active lattice oxygen of PtO_x, Pt−O−Ce linkages, and/or some oxygen species very close to Pt atoms.

proportion of the inactive adsorbed CO intermediates was high on the oxidized Pt sites according to in situ IR analysis. The amount of the most active lattice oxygen of PtO_x clusters decreased according to H_2-TPR and DFT simulations. As a result, some PtO_x sites deactivated during CO oxidation because of the increasing CN(Pt−O) value.

For the sample of PtO_x/CeO_2 NWs-140, it required enough anchoring ligands −O to stabilize Pt atoms that were close to the atomic dispersion limits. The Pt sites with the highest CN(Pt−O) values seemed to be overstabilized by the oxygen linkages and showed the lowest activity. When this sample was reduced with H_2 at 180 °C for some minutes to break some Pt−O bonds according to the H_2-TPR profiles in Figure 3, its catalytic activity increased significantly and could reach a value in the initial minutes of the catalytic tests similar to that exhibited by the active samples of PtO_x/CeO_2 NWs-350 (Figure S24 and Table S5 in the Supporting Information). This is not in conflict with recent reports that single-atom Pt can be very active.[1,2,11] However, in some reports, atomically dispersed metal on inert supports with an initial CN(metal−O) value of about 4 can show high activity with a decrease in CN value when the catalytic reaction begins.[1,2] Our sample of PtO_x/CeO_2 NWs-140 with similar highly dispersed PtO_x clusters showed only low activity, and an increasing CN(Pt−O) caused a decreasing activity of our other samples. These differences are likely to be caused by the role of CeO_2 NWs supports, which tended to increase the oxygen linkages to overstabilize the PtO_x clusters as an exhibition of the atomic level Pt−O−support interactions.

On the basis of the above discussion, an appropriate local coordination structure of Pt sites should be considered for these samples to increase the Pt utilization efficiency. Small CN(Pt−Pt) and CN(Pt−O) values for PtO_x clusters are considered to be helpful to increase the number of total and effective interfacial active sites, respectively, and consequently enhance their catalytic performance.

CONCLUSION

Atoms and clusters of Pt were deposited to form PtO_x clusters on the subnanometric scale on well-defined CeO_2 NWs with a (110) surface. Most of the PtO_x clusters were at the interface and were strongly affected by the metal−support interactions, so that the Pt sites were mainly in the oxidized state and were highly coordinated with oxygen. The catalytic activity of the subnanometer PtO_x clusters on CeO_2 NWs in CO oxidation at low temperature was sensitive to the local coordination structure of the interfacial PtO_x sites. PtO_x clusters with high dispersion provided increased interfacial sites for the catalytic reaction and promoted the activity of the interfacial lattice oxygen close to Pt atoms. Meanwhile, the interfacial Pt sites were favorable in binding oxygen during CO oxidation due to the strong metal−support interactions. Coordinated oxygen with high CN(Pt−O) values tended to overstabilize the Pt atoms and to deactivate the Pt sites. There was a high proportion of unreactive adsorbed CO intermediates on the inactive oxidized Pt sites. Consequently, the amount of the most active lattice oxygens surrounding Pt atoms decreased. With an increasing CN(Pt−O) value, the catalysts lost a part of the effective active sites, which caused decreased catalytic activity. The catalytic efficiency and the Pt utilization could be improved by modulating the samples with a relatively small CN(Pt−O) under the premise of highly exposed Pt sites. This work offers new insights into PtO_x clusters at the subnanometer scale on CeO_2 NWs for CO oxidation from the aspect of local coordination structure effects, which is helpful in understanding the intrinsic properties of this type of active site for the rational design of catalysts with both scientific importance and industrial applications.

ASSOCIATED CONTENT

Supporting Information

The Supporting Information is available free of charge on the ACS Publications website at DOI: 10.1021/acscatal.5b00832.

TEM and STEM images, EXAFS spectra, catalytic properties, and other data (PDF)

AUTHOR INFORMATION

Corresponding Authors

*E-mail for R.S.: sirui@sinap.ac.cn.
*E-mail for H.L.: hcliu@pku.edu.cn.
*E-mail for Y.-W.Z.: ywzhang@pku.edu.cn.

Notes

The authors declare no competing financial interest.

DOI: 10.1021/acscatal.5b00832
ACS Catal. 2015, 5, 5164−5173

■ ACKNOWLEDGMENTS

This work was supported by the National Science Foundation of China (NSFC) (grant nos. 21025101, 21271011, 21321001, 21173008, 21373259, and 21331001). Y.-W.Z. particularly appreciates the financial aid of China National Funds for Distinguished Young Scientists from the NSFC. R.S. acknowledges support from the Hundred Talents project of the Chinese Academy of Sciences and the Strategic Priority Research Program of the Chinese Academy of Sciences (grant no. XDA09030102). The work on microscopy was partially carried out at the Center of Electron Microscopy of Zhejiang University, which is financially supported by the NSFC (51222202 and 51472215), the National Basic Research Program of China (2014CB932500), the Program for Innovative Research Team in University of Ministry of Education of China (IRT13037), and the Fundamental Research Funds for the Central Universities (2014XZZX003-07 and 2015CB92100). We thank Nebojsa Marinkovic (University of Delaware) for his help on the in situ XAFS setups and the beamline staff (1W2B of BSRF and BL14W1 of SSRF) for their aid in the ex situ XAFS measurements. We highly appreciate the reviewers for their constructive suggestions, which helped us improve our work. We also thank Dr. Shuo-Ren Du for his help in revising this paper.

■ REFERENCES

(1) Yang, M.; Liu, J.; S, L.; Zugic, B.; Huang, J.; Allard, L. F.; Flytzani-Stephanopoulos, M. *J. Am. Chem. Soc.* **2015**, *137*, 3470−3473.
(2) Peterson, E. J.; Delariva, A. T.; Lin, S.; Johnson, R. S.; Guo, H.; Miller, J. T.; Kwak, J. H.; Peden, C. H. F.; Kiefer, B.; Allard, L. F.; Ribeiro, F. H.; Datye, A. K. *Nat. Commun.* **2014**, *5*, 4885.
(3) Flytzani-Stephanopoulos, M.; Gates, B. C. *Annu. Rev. Chem. Biomol. Eng.* **2012**, *3*, 545−574.
(4) Song, H. *Acc. Chem. Res.* **2015**, *48*, 491−499.
(5) Bhan, A.; Iglesia, E. *Acc. Chem. Res.* **2008**, *41*, 559−567.
(6) Ke, J.; Xiao, J. W.; Zhu, W.; Liu, H. C.; Si, R.; Zhang, Y. W.; Yan, C. H. *J. Am. Chem. Soc.* **2013**, *135*, 15191−15200.
(7) Bruix, A.; Lykhach, Y.; Matolinova, I.; Neitzel, A.; Skala, T.; Tsud, N.; Vorokhta, M.; Stetsovych, V.; Sevcikova, K.; Myslivecek, J.; Fiala, R.; Vaclavu, M.; Prince, K. C.; Bruyere, S.; Potin, V.; Illas, F.; Matolin, V.; Libuda, J.; Neyman, K. M. *Angew. Chem., Int. Ed.* **2014**, *53*, 10525−10530.
(8) Yu, W. T.; Porosoff, M. D.; Chen, J. G. G. *Chem. Rev.* **2012**, *112*, 5780−5817.
(9) Ertl, G.; Knözinger, H.; Schüth, F.; Weitkamp, J. *Handbook of Heterogeneous Catalysis*, 2nd ed.; Wiley-VCH: Weinheim, Germany, 2008; pp 81−119.
(10) Yam, V. W. W. *Nat. Chem.* **2010**, *2*, 791−791.
(11) Qiao, B. T.; Wang, A. Q.; Yang, X. F.; Allard, L. F.; Jiang, Z.; Cui, Y. T.; Liu, J. Y.; Li, J.; Zhang, T. *Nat. Chem.* **2011**, *3*, 634−641.
(12) Qiao, B. T.; Wang, A. Q.; Li, L.; Lin, Q. Q.; Wei, H. S.; Liu, J. Y.; Zhang, T. *ACS Catal.* **2014**, *4*, 2113−2117.
(13) Lee, S.; Fan, C.; Wu, T.; Anderson, S. L. *J. Am. Chem. Soc.* **2004**, *126*, 5682−5683.
(14) Wei, H. S.; Liu, X. Y.; Wang, A. Q.; Zhang, L. L.; Qiao, B. T.; Yang, X. F.; Huang, Y. Q.; Miao, S.; Liu, J. Y.; Zhang, T. *Nat. Commun.* **2014**, *5*, 5634.
(15) Kistler, J. D.; Chotigkrai, N.; Xu, P. H.; Enderle, B.; Praserthdam, P.; Chen, C. Y.; Browning, N. D.; Gates, B. C. *Angew. Chem., Int. Ed.* **2014**, *53*, 8904−8907.
(16) Kuwauchi, Y.; Takeda, S.; Yoshida, H.; Sun, K.; Haruta, M.; Kohno, H. *Nano Lett.* **2013**, *13*, 3073−3077.
(17) Ta, N.; Liu, J. J.; Chenna, S.; Crozier, P. A.; Li, Y.; Chen, A.; Shen, W. *J. Am. Chem. Soc.* **2012**, *134*, 20585−20588.
(18) Vayssilov, G. N.; Lykhach, Y.; Migani, A.; Staudt, T.; Petrova, G. P.; Tsud, N.; Skala, T.; Bruix, A.; Illas, F.; Prince, K. C.; Matolin, V.; Neyman, K. M.; Libuda, J. *Nat. Mater.* **2011**, *10*, 310−315.
(19) Royer, S.; Duprez, D. *ChemCatChem* **2011**, *3*, 24−65.
(20) Meng, L.; Jia, A.-P.; Lu, J.-Q.; Luo, L.-F.; Huang, W.-X.; Luo, M.-F. *J. Phys. Chem. C* **2011**, *115*, 19789−19796.
(21) Zhang, C.; Michaelides, A.; King, D. A.; Jenkins, S. J. *J. Am. Chem. Soc.* **2010**, *132*, 2175−2182.
(22) Yoshida, H.; Nonoyama, S.; Yazawa, Y.; Hattori, T. *Catal. Today* **2010**, *153*, 156−161.
(23) Camellone, M. F.; Fabris, S. *J. Am. Chem. Soc.* **2009**, *131*, 10473−10483.
(24) Grass, M. E.; Zhang, Y.; Butcher, D. R.; Park, J. Y.; Li, Y.; Bluhm, H.; Bratlie, K. M.; Zhang, T.; Somorjai, G. A. *Angew. Chem., Int. Ed.* **2008**, *47*, 8893−8896.
(25) Nagai, Y.; Hirabayashi, T.; Dohmae, K.; Takagi, N.; Minami, T.; Shinjoh, H.; Matsumoto, S. *J. Catal.* **2006**, *242*, 103−109.
(26) Kwak, J. H.; Hu, J.; Mei, D.; Yi, C. W.; Kim do, H.; Peden, C. H.; Allard, L. F.; Szanyi, J. *Science* **2009**, *325*, 1670−1673.
(27) Yang, M.; Li, S.; Wang, Y.; Herron, J. A.; Xu, Y.; Allard, L. F.; Lee, S.; Huang, J.; Mavrikakis, M.; Flytzani-Stephanopoulos, M. *Science* **2014**, *346*, 1498−1501.
(28) Bruix, A.; Rodriguez, J. A.; Ramirez, P. J.; Senanayake, S. D.; Evans, J.; Park, J. B.; Stacchiola, D.; Liu, P.; Hrbek, J.; Illas, F. *J. Am. Chem. Soc.* **2012**, *134*, 8968−8974.
(29) Park, J. B.; Graciani, J.; Evans, J.; Stacchiola, D.; Ma, S.; Liu, P.; Nambu, A.; Sanz, J. F.; Hrbek, J.; Rodriguez, J. A. *Proc. Natl. Acad. Sci. U. S. A.* **2009**, *106*, 4975−4980.
(30) Trovarelli, A. *Catal. Rev.: Sci. Eng.* **1996**, *38*, 439−520.
(31) Vivier, L.; Duprez, D. *ChemSusChem* **2010**, *3*, 654−678.
(32) Glaspell, G.; Hassan, H. M. A.; Elzatahry, A.; Abdalsayed, V.; El-Shall, M. S. *Top. Catal.* **2008**, *47*, 22−31.
(33) Zhou, K. B.; Wang, X.; Sun, X. M.; Peng, Q.; Li, Y. D. *J. Catal.* **2005**, *229*, 206−212.
(34) Kim, H. Y.; Henkelman, G. *J. Phys. Chem. Lett.* **2013**, *4*, 216−221.
(35) Wu, Z.; Li, M.; Overbury, S. H. *J. Catal.* **2012**, *285*, 61−73.
(36) Lee, Y.; He, G.; Akey, A. J.; Si, R.; Flytzani-Stephanopoulos, M.; Herman, I. P. *J. Am. Chem. Soc.* **2011**, *133*, 12952−12955.
(37) Guzman, J.; Carrettin, S.; Corma, A. *J. Am. Chem. Soc.* **2005**, *127*, 3286−3287.
(38) Yamamoto, T.; Suzuki, A.; Nagai, Y.; Tanabe, T.; Dong, F.; Inada, Y.; Nomura, M.; Tada, M.; Iwasawa, Y. *Angew. Chem., Int. Ed.* **2007**, *46*, 9253−9256.
(39) Trovarelli, A. *Catalysis by Ceria and Related Materials*; Impreial College Press: London, 2002; pp 15−168.
(40) Vayssilov, G. N.; Migani, A.; Neyman, K. *J. Phys. Chem. C* **2011**, *115*, 16081−16086.
(41) Polster, C. S.; Zhang, R.; Cyb, M. T.; Miller, J. T.; Baertsch, C. D. *J. Catal.* **2010**, *273*, 50−58.
(42) Hadjiivanov, K. I.; Vayssilov, G. N. *Adv. Catal.* **2002**, *47*, 307−511.
(43) Fu, Q.; Li, W. X.; Yao, Y. X.; Liu, H. Y.; Su, H. Y.; Ma, D.; Gu, X. K.; Chen, L. M.; Wang, Z.; Zhang, H.; Wang, B.; Bao, X. H. *Science* **2010**, *328*, 1141−1144.
(44) Yoon, K.; Yang, Y.; Lu, P.; Wan, D.; Peng, H. C.; Stamm Masias, K.; Fanson, P. T.; Campbell, C. T.; Xia, Y. *Angew. Chem., Int. Ed.* **2012**, *51*, 9543−9546.
(45) Cargnello, M.; Doan-Nguyen, V. V.; Gordon, T. R.; Diaz, R. E.; Stach, E. A.; Gorte, R. J.; Fornasiero, P.; Murray, C. B. *Science* **2013**, *341*, 771−773.
(46) Gao, Y.; Wang, W.; Chang, S.; Huang, W. *ChemCatChem* **2013**, *5*, 3610−3620.
(47) Lin, F.; Hoang, D. T.; Tsung, C.-K.; Huang, W.; Lo, S. H.-Y.; Wood, J. B.; Wang, H.; Tang, J.; Yang, P. *Nano Res.* **2011**, *4*, 61−71.
(48) Singhania, N.; Anumol, E. A.; Ravishankar, N.; Madras, G. *Dalton Trans.* **2013**, *42*, 15343−15354.
(49) Liu, H.-H.; Wang, Y.; Jia, A.-P.; Wang, S.-Y.; Luo, M.-F.; Lu, J.-Q. *Appl. Surf. Sci.* **2014**, *314*, 725−734.
(50) Nolan, M. *J. Chem. Phys.* **2012**, *136*, 134703.
(51) Nolan, M.; Parker, S. C.; Watson, G. W. *Surf. Sci.* **2005**, *595*, 223−232.
(52) Castleton, C. W.; Kullgren, J.; Hermansson, K. *J. Chem. Phys.* **2007**, *127*, 244704.

DOI: 10.1021/acscatal.5b00832
ACS Catal. 2015, 5, 5164−5173

(53) Alexeev, O. S.; Li, F.; Amiridis, M. D.; Gates, B. C. *J. Phys. Chem. B* **2005**, *109*, 2338−2349.
(54) Bunluesin, T.; Putna, E. S.; Gorte, R. J. *Catal. Lett.* **1996**, *41*, 1−5.
(55) Zafiris, G. S.; Gorte, R. J. *J. Catal.* **1993**, *143*, 86−91.
(56) Yao, H. C.; Yao, Y. F. Y. *J. Catal.* **1984**, *86*, 254−265.
(57) Lin, W.; Herzing, A. A.; Kiely, C. J.; Wachs, I. E. *J. Phys. Chem. C* **2008**, *112*, 5942−5951.
(58) Daniel, D. W. *J. Phys. Chem.* **1988**, *92*, 3891−3899.
(59) Carlsson, P.; Osterlund, L.; Thormahlen, P.; Palmqvist, A.; Fridell, E.; Jansson, J.; Skoglundh, M. *J. Catal.* **2004**, *226*, 422−434.
(60) Pozdnyakova, O.; Teschner, D.; Wootsch, A.; Krohnert, J.; Steinhauer, B.; Sauer, H.; Toth, L.; Jentoft, F.; Knopgericke, A.; Paal, Z. *J. Catal.* **2006**, *237*, 1−16.
(61) Bera, P.; Gayen, A.; Hegde, M. S.; Lalla, N. P.; Spadaro, L.; Frusteri, F.; Arena, F. *J. Phys. Chem. B* **2003**, *107*, 6122−6130.
(62) Jin, T.; Zhou, Y.; Mains, G. J.; White, J. M. *J. Phys. Chem.* **1987**, *91*, 5931−5937.
(63) Bazin, P.; Saur, O.; Lavalley, J. C.; Daturi, M.; Blanchard, G. *Phys. Chem. Chem. Phys.* **2005**, *7*, 187−194.
(64) Martinez-Arias, A.; Coronado, J. M.; Cataluna, R.; Conesa, J. C.; Soria, J. *J. Phys. Chem. B* **1998**, *102*, 4357−4365.
(65) Perrichon, V. *Appl. Catal., A* **2004**, *260*, 1−8.
(66) Alexeev, O. S.; Chin, S. Y.; Engelhard, M. H.; Ortiz-Soto, L.; Amiridis, M. D. *J. Phys. Chem. B* **2005**, *109*, 23430−23443.
(67) Negreiros, F. R.; Fabris, S. *J. Phys. Chem. C* **2014**, *118*, 21014−21020.
(68) Hatanaka, M.; Takahashi, N.; Tanabe, T.; Nagai, Y.; Dohmae, K.; Aoki, Y.; Yoshida, T.; Shinjoh, H. *Appl. Catal., B* **2010**, *99*, 336−342.

DOI: 10.1021/acscatal.5b00832
ACS Catal. 2015, 5, 5164−5173